

Extracellular Stimulation of Central Neurons: Influence of Stimulus Waveform and Frequency on Neuronal Output

CAMERON C. MCINTYRE AND WARREN M. GRILL

Department of Biomedical Engineering, Case Western Reserve University, Cleveland, Ohio 44106-4912

Received 28 February 2002; accepted in final form 26 June 2002

McIntyre, Cameron C., and Warren M. Grill. Extracellular stimulation of central neurons: influence of stimulus waveform and frequency on neuronal output. *J Neurophysiol* 88: 1592–1604, 2002; 10.1152/jn.00147.2002. The objective of this project was to examine the influence of stimulus waveform and frequency on extracellular stimulation of neurons with their cell bodies near the electrode (local cells) and fibers of passage in the CNS. Detailed computer-based models of CNS cells and axons were developed that accurately reproduced the dynamic firing properties of mammalian motoneurons including afterpotential shape, spike-frequency adaptation, and firing frequency as a function of stimulus amplitude. The neuron models were coupled to a three-dimensional finite element model of the spinal cord that solved for the potentials generated in the tissue medium by an extracellular electrode. Extracellular stimulation of the CNS with symmetrical charge balanced biphasic stimuli resulted in activation of fibers of passage, axon terminals, and local cells around the electrode at similar thresholds. While high stimulus frequencies enhanced activation of fibers of passage, a much more robust technique to achieve selective activation of targeted neuronal populations was via alterations in the stimulus waveform. Asymmetrical charge-balanced biphasic stimuli, consisting of a long-duration low-amplitude cathodic prepulse phase followed by a short-duration high-amplitude anodic stimulus phase, enabled selective activation of local cells. Conversely, an anodic prepulse phase followed by a cathodic stimulus phase enabled selective activation of fibers of passage. The threshold for activation of axon terminals in the vicinity of the electrode was lower than the threshold for direct activation of local cells, independent of the stimulus waveform. As a result, stimulation induced *trans*-synaptic influences (indirect depolarization/hyperpolarization) on local cells altered their neural output, and this indirect effect was dependent on stimulus frequency. If the indirect activation of local cells was inhibitory, there was little effect on the stimulation induced neural output of the local cells. However, if the indirect activation of the local cells was excitatory, attempts to activate selectively fibers of passage over local cells was limited. These outcomes provide a biophysical basis for understanding frequency-dependent outputs during CNS stimulation and provide useful tools for selective stimulation of the CNS.

INTRODUCTION

Microstimulation in the CNS can activate populations of neurons with greater specificity than is possible with larger electrodes on the surface of the spinal cord or brain (Gustafsson and Jankowska 1976; Ranck 1975). The potential thus arises for electrical activation of intact neuronal circuitry and, in turn, generation of distributed and controlled motor outputs

for the study of the neural control of movement (Giszter et al. 1993) or for application in neural prostheses (Barbeau et al. 1999). Knowing what neural elements are activated by the stimulus is of fundamental importance in understanding the behavioral response, and in the case of neural prostheses, selective activation of targeted populations is required for device efficacy. However, in many regions of the CNS, local cells and fibers of passage are intermingled in close proximity to the electrode, and their thresholds are similar with conventional stimuli (McIntyre and Grill 1999, 2000; Ranck 1975).

We have previously developed asymmetric biphasic charge-balanced stimuli that increased the threshold difference between neurons with their cell bodies near the electrode (local cells) and fibers of passage (McIntyre and Grill 2000). However, this analysis was limited to idealized neural orientations and single stimuli. The first goal of the present study was to determine if asymmetric biphasic charge-balanced stimulus waveforms are effective in increasing the selectivity between cells and fibers in a specific instance of intraspinal microstimulation. The second goal was to determine if the waveforms are effective under repetitive activation with trains of stimuli. Our hypothesis was that stimulus trains would provide enhanced selectivity because of differences in the post-action potential excitability of cells and fibers of passage. In addition to the direct influence of the stimulus, an indirect influence can also affect the activation of local cells. This indirect influence arises from the excitation of presynaptic neural elements by the stimulus pulse, and their subsequent postsynaptic effects on local cells that can influence neural output (Baldissera et al. 1972; Gustafsson and Jankowska 1976). Therefore the third goal of this study was to quantify the effects of stimulation induced *trans*-synaptic inputs on extracellular activation of local cells.

We developed a computer-based integrated field-neuron model to study the influence of stimulus waveform and frequency on selectivity between cells and fibers of passage. The field-neuron model consisted of the extracellular electric field computed using a finite element model of microstimulation of the spinal cord, coupled to multi-compartment neuron models to determine the effects of extracellular stimulation on neural output. We modeled stimulation near Onuf's nucleus in the sacral region of the cat spinal cord as this provides a system amenable to experimental testing of the model predictions and

Address for reprint requests: W. M. Grill, Case Western Reserve University, Dept. of Biomedical Engineering, C.B. Bolton Bldg., Rm. 3480, Cleveland, OH 44106-4912 (E-mail: wmg@po.cwru.edu).

The costs of publication of this article were defrayed in part by the payment of page charges. The article must therefore be hereby marked "advertisement" in accordance with 18 U.S.C. Section 1734 solely to indicate this fact.

is an area targeted for stimulation for restoration of bladder emptying (Grill et al. 1999; Prochazka et al. 2001). The axons of the preganglionic parasympathetic innervation of the bladder run in close proximity to the cell bodies of the somatic motoneurons innervating the external urethral sphincter (Nadelhaft et al. 1980; Thor et al. 1989; Vanderhorst and Holstege 1997). Contraction of the bladder and external urethral sphincter can be measured to determine activation of fibers and local cells, respectively. Therefore building our model around this physiological system will enable experimental testing of the model-designed stimulus parameters.

The influence of extracellular electric fields on neurons is related to the second difference of the extracellular potential along the extent of the individual neurons and will cause both regions of depolarization and regions of hyperpolarization in the same neuron (Basser and Roth 2000). Cathodic or anodic stimuli result in different sites of action potential initiation (API) in local cells and fibers of passage (McIntyre and Grill 1999). In general, when stimulating local cells, API occurs in the axon of the neuron, relatively far from the electrode, whereas when stimulating fibers of passage, API occurs in a region of the fiber relatively close to the electrode. Previous modeling and experimental work has shown that local cells have lower thresholds for activation with anodic stimuli, whereas fibers of passage have lower thresholds with cathodic stimuli (McIntyre and Grill 1999, 2000; Ranck 1975). However, chronic application of electrical stimulation within the nervous system requires the use of biphasic stimuli because of issues related to tissue damage and electrode corrosion (Pudenz et al. 1975). When biphasic stimuli are used, local cells and fibers of passage will be activated during the anodic and cathodic phases of the stimulus, respectively, resulting in low selectivity for activation of a target population (McIntyre and Grill 2000).

The objectives of this study were to examine the influence of stimulus waveform and frequency on extracellular stimulation of local cells and fibers of passage and to develop techniques that may be effective in generating selective activation of either population. The results demonstrate that the appropriate choice of stimulus waveform and frequency, based on differences between the geometrical and electrical properties of fibers of passage and local cells, provide effective techniques to enable selective activation of targeted neural populations when using microstimulation in the CNS. The results also indicate that when activating local cells near the electrode, the threshold for excitation of presynaptic inputs is less than the threshold for direct activation of the postsynaptic cells. As a result, the stimulus train can generate postsynaptic potentials in local cells that can play a role in their excitability.

METHODS

An integrated field-neuron model was developed to study neural activation by extracellular stimulation with microelectrodes within the spinal cord. A three-dimensional finite-element model of the spinal cord was used to solve for the potentials generated in the tissue by microstimulation. The resulting extracellular potentials were applied to detailed multi-compartment neural models used to represent the geometrical and electrical properties of both myelinated fibers of passage and motoneurons (including a branching dendritic tree, soma, initial segment and myelinated axon) to create an integrated field-neuron model.

Fiber model

The multi-compartment cable model of the myelinated axon, described in detail in McIntyre et al. (2002), contained 10 segments between successive nodes with an explicit representation of the myelin attachment segment (MYSA), paranode main segment (FLUT), and internode segment (STIN) regions of the fiber (Fig. 1; Tables 1 and 2; APPENDIX). The double-cable structure incorporated both linear and nonlinear membrane dynamics to represent the electrical behavior of the fiber. The nodes consisted of the parallel combination of nonlinear fast Na^+ , persistent Na^+ , and slow K^+ conductances, a linear leakage conductance, and the membrane capacitance. The paranodal and internodal compartments included two concentric layers, each including a linear conductance in parallel with the membrane capacitance, to represent the myelin sheath and underlying axolemma. The myelinated axon model reproduced a wide range of experimental data including the strength-duration relationship, current-distance relationship, conduction velocity, afterpotential shape, and changes in excitability after a single or train of stimuli (McIntyre et al. 2002).

Motoneuron model

The cell body, consisting of the soma and axon initial segment, was modeled as a three-dimensional structure using nine compartments with geometries based on morphological data (Cullheim and Kellerth 1978; Cullheim et al. 1987; Sasaki 1994). Motoneuron models traditionally represent the soma as one spherical compartment; however, the soma is a geometrically complex structure with tapering attachments to its processes. Therefore we developed a distributed soma model (McIntyre and Grill 2000) with six tapering cylinders where the large end of each tapered compartment connected to the other soma compartments and the small end of each tapered compartment connected to one of the five dendrites or the initial segment (Fig. 1; Table 1). The soma had a total membrane surface area of $4,920 \mu\text{m}^2$. The initial segment of the axon was modeled with three cylindrical compartments connected in series.

The soma included conductances representing nonlinear fast Na^+ ,

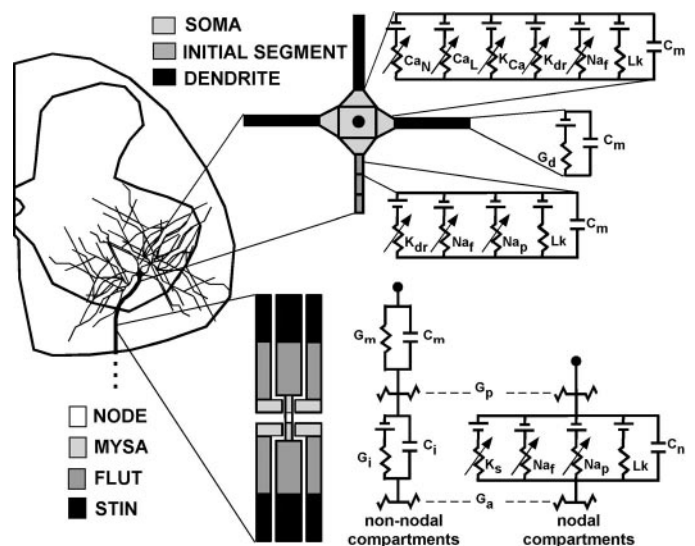


FIG. 1. Multi-compartment cable model of a motoneuron. The model consisted of a 3-dimensional branching dendritic tree, multi-compartment soma and initial segment, and a myelinated axon with explicit representation of the myelin and underlying axolemma (see text for abbreviations). The soma, initial segment, and nodes of Ranvier used nonlinear membrane dynamics derived from voltage- and current-clamp measurements on mammalian neurons. Intracellular resistors, determined by the dimensions of the adjoining compartments, connected the different elements of the model together.

TABLE 1. Model geometric parameters (μm)

Cell body	
Soma compartment length ^{a-c}	15
Soma compartment diameter ^{a-d}	7:35 ^e
Soma compartment diameter ^{a-c,f}	4:35 ^e
Initial segment compartment length ^{g,h,c}	10
Initial segment diameter ^{g,h,c}	4
Myelinated axon ⁱ	
Fiber diameter	11.5
Number of myelin lamella	130
Node length	1
Node diameter	3.7
MYSA length	3
MYSA diameter	3.7
MYSA periaxonal space width	0.002
FLUT length	50
FLUT diameter	8.1
FLUT periaxonal space width	0.004
STIN length (first 4 internodes) ^j	63.5
STIN length (last 6 internodes) ^j	190.5
STIN diameter	8.1
STIN periaxonal space width	0.004

MYSA, myelin attachment segment. ^a Six total soma compartments; ^b Cullheim et al. (1987); ^c Sasaki (1994); ^d compartments attached to dendrites; ^e linear increase from initial diameter to final diameter; ^f compartment attached to initial segment; ^g 3 total initial segment compartments; ^h Cullheim and Kellerth (1978); ⁱ myelinated axon references and notes in McIntyre et al. (2002); ^j Fabricius et al. (1994).

N-type Ca^{2+} , L-type Ca^{2+} , delayed rectifier K^{+} , and Ca^{2+} -activated K^{+} channels as well as a linear leakage conductance all in parallel with the membrane capacitance (Fig. 1; Tables 3 and 4; APPENDIX). The initial segment included conductances representing nonlinear fast Na^{+} , persistent Na^{+} , and delayed rectifier K^{+} channels as well as a linear leakage conductance all in parallel with the membrane capacitance (Fig. 1; Tables 3 and 4; APPENDIX). The somatic conductances are analogous to those originally identified and described experimentally by Barrett et al. (1980) and Barrett and Crill (1980) for cat motoneurons in addition to the N- and L-type Ca^{2+} conductances that regulate the Ca^{2+} -activated K^{+} conductance (Hounsgaard and Mintz 1988). The initial segment also contained a persistent sodium conductance based on recent work suggesting its pivotal role in action potential initiation (Lee and Heckman 2001).

The dendritic geometry of the model was based on the three-dimensional distribution of dendrites of type-identified alpha-motoneurons, labeled intracellularly with horseradish peroxidase (HRP) (Cullheim et al. 1987; Sasaki 1994), and was modeled with 535 compartments each using linear membrane dynamics that consisted of a linear leakage conductance in parallel with the membrane capacitance (Fig. 1; Table 4). The model had five identical root dendrites

TABLE 2. Axon electrical parameters

Axon internode parameters*	
Myelin conductance (g_m), S/cm^2	0.001
Myelin capacitance (c_m), $\mu\text{F}/\text{cm}^2$	0.1
MYSA conductance (g_a), S/cm^2	0.001
FLUT conductance (g_l), S/cm^2	0.0001
STIN conductance (g_i), S/cm^2	0.0001
Reversal potential (E_{Lk}), mV	-70.0
Axon node parameters*	
Maximum fast Na^{+} conductance (g_{Naf}), S/cm^2	3.0
Maximum slow K^{+} conductance (g_{Ks}), S/cm^2	0.08
Maximum persistent Na^{+} conductance (g_{Nap}), S/cm^2	0.01
Leakage conductance (g_{Lk}), S/cm^2	0.007
Na^{+} Nernst potential (E_{Na}), mV	60.0
K^{+} Nernst potential (E_{K}), mV	-80.0
Leakage reversal potential (E_{Lk}), mV	-80.0

* Myelinated axon references and notes in McIntyre et al. (2002).

TABLE 3. General model electrical parameters

Neuron rest potential (V_{rest}), mV	-70.0
Membrane capacitance (c_m), $\mu\text{F}/\text{cm}^2$	2
Cell body intracellular resistivity (ρ_{cb}), $\Omega\text{ cm}$	200
Dendrite intracellular resistivity (ρ_{dend}), $\Omega\text{ cm}$	200
Axon intracellular resistivity (ρ_a), $\Omega\text{ cm}$	70
Periaxonal resistivity (ρ_p), $\Omega\text{ cm}$	70

that originated at the soma. Each root dendrite had an arbor based on the results presented in Fig. 1 of Cullheim et al. (1987), with a root diameter of 7 μm and 25 terminations. The total dendritic arbor had 125 terminations and a surface area of 269,980 μm^2 .

Spinal cord model

A three-dimensional finite-element model (FEM) was used to create an anatomically and electrically accurate volume conductor model of the cat sacral spinal cord (Miller and Henriquez 1990) (Fig. 2). The model geometry was derived from the histological data of Vanderhorst and Holstege (1997), who described the gray-and-white matter geometry as well as the anatomical location of the motoneurons innervating each of the muscle groups originating in the lumbosacral spinal cord. The white matter was modeled as two-dimensionally anisotropic with a longitudinal conductivity of 0.0033 S/cm and a transverse conductivity of 0.00083 S/cm based on previous measurements in the dorsal columns (Ranck and BeMent 1965). The gray matter was modeled as isotropic with a conductivity of 0.002 S/cm as measured for cortical gray matter (Li et al. 1968; Ranck 1963). Surrounding the spinal cord was a layer of saline (0.02 S/cm).

The FEM represented the sacral spinal cord from the S_1 through the S_3 segments and consisted of 91,840 elements. The FEM was implemented in a commercially available finite-element software program, ANSYS 5.7 (ANSYS, Houston, PA) that used a frontal solution method (direct elimination solver) (Irons 1970) of the Laplace equation

$$\nabla \cdot \sigma \nabla \Phi = 0 \quad (1)$$

where the output of the FEM model was the potential (Φ) at each node of the finite-element mesh (Fig. 2). Within 500 μm of the electrode, separation between the nodes of the finite element mesh was $<50\text{ }\mu\text{m}$, and at regions farther from the electrode, progressively larger element sizes were used (Fig. 2D). The potential at the boundary of the model was set to zero and was far enough from the central region of the model that the potentials in the gray-and-white matter differed by $<1\%$ when the distance from the center of the model to the boundary

TABLE 4. Cell body and dendrite electrical parameters

Na^{+} Nernst potential (E_{Na}), mV	50.0
K^{+} Nernst potential (E_{K}), mV	-80.0
Leakage reversal potential (E_{Lk}), mV	-70.0
Soma parameters	
Maximum Na^{+} conductance ^{a-c} (g_{Na}), S/cm^2	0.05
Maximum delayed rectifier K^{+} conductance (g_{Kdr}), S/cm^2	0.3
Maximum N-type Ca^{2+} conductance (g_{CaN}), S/cm^2	0.05
Maximum L-type Ca^{2+} conductance (g_{CaL}), S/cm^2	0.0001
Maximum Ca^{2+} activated K^{+} conductance ($g_{\text{K(Ca)}}$), S/cm^2	0.3
Leakage conductance ^{d,e} (g_{Lk}), S/cm^2	0.002
Initial segment parameters	
Maximum Na^{+} conductance ^{a-c} (g_{Na}), S/cm^2	0.5
Maximum K^{+} conductance (g_{K}), S/cm^2	0.1
Leakage conductance (g_{Lk}), S/cm^2	0.01
Dendrite parameters	
Leakage conductance ^{d,e} (g_{Lk}), S/cm^2	0.0002

^a Safronov et al. (1997); ^b Catterall (1981); ^c Traub and Llinas (1977);

^d Clements and Redman (1989); ^e Fleshman et al. (1988).

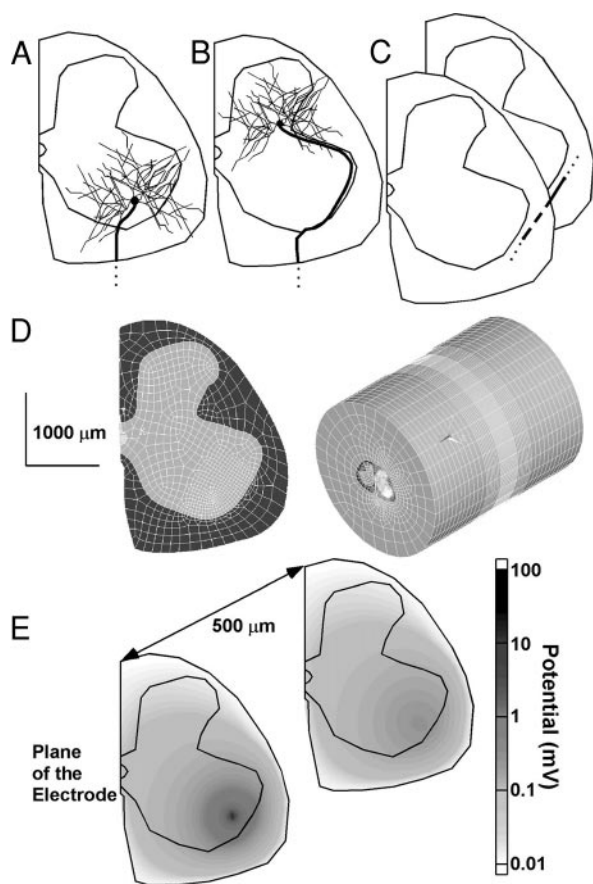


FIG. 2. Integrated model of the spinal cord and spinal neurons. The neuron models were used to represent a motoneuron innervating the external urethral sphincter (A), a preganglionic parasympathetic neuron innervating the bladder (B), and a fiber of passage in the white matter (C). D: a finite-element model, incorporating the inhomogenous and anisotropic electrical properties of the spinal cord, was used to solve for the potential distribution generated by microstimulation in the ventral horn. A nonuniform mesh, both transversely and longitudinally, was used to improve the accuracy near the electrode where the gradient of the electric field was the greatest. E: potential distribution generated in the finite-element model of the spinal cord by a point source of current ($1 \mu\text{A}$). The standard electrode location was in the ventral horn, marked by the point of maximum potential on the "plane of the electrode" potential distribution map. A potential distribution map is also shown for a plane displaced $500 \mu\text{m}$ from the electrode to illustrate the decay of the potential in the longitudinal direction.

was doubled. Point-source electrodes were implemented by assigning currents to the appropriate nodes in the finite-element mesh. The simplification of using point-source electrodes to represent the potential distribution generated by metal microelectrodes is justified from our previous work demonstrating that neural activation produced by a point source was indistinguishable from that produced by sharp tipped microelectrodes (McIntyre and Grill 2001). The FEM was validated by comparing the model solution with homogeneous isotropic conductivities to that of a theoretical point source with $<1\%$ error. Because the bulk conductivity of the cord is linear, the potential distributions for different stimulus current magnitudes were scaled versions of the potential distribution generated by a unitary current stimulus (Hulbert and Tator 1993; Nicholson and Freeman 1975).

Simulations with the integrated spinal cord and neuron models

The neuron models were positioned within the volume conductor model of the spinal cord at locations based to experimental tracing

studies (Nadelhaft et al. 1980; Thor et al. 1989; Vanderhorst and Holstege 1997) (Fig. 2, A–C). The output of the FEM was the potential at each node of the finite-element mesh; however, the location of the nodes of the mesh did not necessarily correspond to the location of a given neuronal compartment. Therefore three-dimensional tessellation-based linear interpolation was used to determine the potential between points in the finite-element mesh (Watson 1999). The extracellular potentials generated by the stimulus were applied to the neuron models, and an equivalent set of distributed intracellular injected currents was calculated and used to stimulate the neurons (McIntyre and Grill 2000, 2001; Richardson et al. 2000; Warman et al. 1992).

All simulations (except for data presented in Fig. 3) used a standard electrode location in the ventral horn of the spinal cord (Fig. 2, D and E). This electrode location enabled comparison among the outputs of three populations of neurons activated by extracellular sources: neurons with their cell bodies near the electrode representing the somatic motoneurons controlling the external urethral sphincter (EUS) (Fig. 2A), neurons with their axons passing by the electrode but with their cell bodies within $\sim 1,000 \mu\text{m}$ of the electrode representing the parasympathetic preganglionic neurons controlling the bladder (BLA) (Fig. 2B), and neurons with their axons passing by the electrode but with their cell bodies far from the electrode representing fibers of passage in the white matter (FOP) (Fig. 2C). The threshold for excitation with a single symmetrical, charge-balanced, cathodic first, biphasic stimulus 0.1 ms in duration (each phase) was $34 \mu\text{A}$ for all three models at the standard ventral horn electrode position (Fig. 2, D and E). This enabled comparison of changes in the neuronal output with alteration in the stimulus frequency and stimulus waveform from a reference point that represented the most commonly used stimulus waveform in neuroprosthetic applications.

RESULTS

We used an integrated model of the electric field generated by intraspinal microstimulation coupled to multi-compartment cable models of spinal neurons to study activation of CNS neurons by extracellular stimulation. The multi-compartment cable models were able to replicate a wide range of experimental data on the excitation properties of mammalian neurons, and the output of the integrated field-neuron model agreed qualitatively with responses generated by microstimulation of the sacral spinal cord. Asymmetric biphasic stimulus waveforms enabled selective activation of either cells near the electrode or fibers of passage during repetitive activation. Alterations in stimulus frequency, which exploited differences in the post-action potential excitabilities of the neuronal cell bodies and the fibers of passage, could also increase selectivity. In addition, the results indicate that stimulation induced *trans-synaptic* excitation/inhibition of local cells influenced the neuronal output during repetitive extracellular stimulation.

Dynamic firing properties of the neuron model

The motoneuron model was able to reproduce several independent sets of experimental data from mammalian motoneurons (Fig. 3). The action potential recorded in the soma had a magnitude and shape that matched well with experimental data (Barrett et al. 1980), and the depolarizing (DAP) and hyperpolarizing (AHP) afterpotentials had amplitudes and durations similar to in vivo recordings (Zengel et al. 1985) (Fig. 3A). The dynamic firing properties of the neuron model matched well with experimental recordings. When a constant current intracellular stimulus was applied

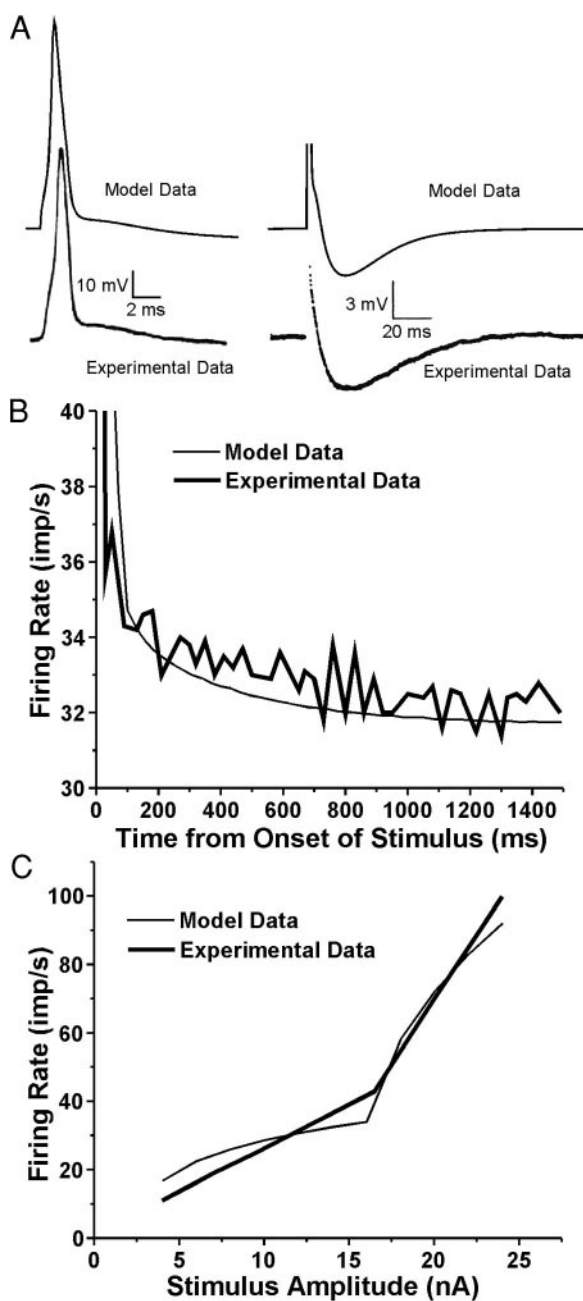


FIG. 3. Comparison of the excitation properties of the motoneuron model to experimental data. *A*: somatic action potential spike and depolarizing afterpotential of the model motoneuron compared with experimental data from cat (Barrett et al. 1980). Somatic afterhyperpolarization of the model motoneuron compared with experimental data from cat (Zengel et al. 1985) (action potentials truncated). *B*: somatic firing frequency as a function of time for a constant current stimulus (13.5 nA) compared with experimental data from rat (Sawczuk et al. 1995). *C*: somatic steady-state firing frequency as a function of constant current stimulus amplitude applied in the soma for the model compared with experimental data from cat (Schwindt and Grill 1982).

to the soma, the model exhibited spike-frequency adaptation that had a time course similar to experimental data (Sawczuk et al. 1995) (Fig. 3*B*). The steady-state firing rate of the motoneuron model as a function of the amplitude of the intracellular stimulus exhibited primary and secondary firing ranges that also matched well with experimental data (Schwindt and Grill 1982) (Fig. 3*C*).

Model comparison to spinal cord microstimulation experiments

The threshold current as a function of the electrode-to-neuron distance for the model motoneuron innervating the EUS was compared with the experimental measurements from Gustafsson and Jankowska (1976) (Fig. 4*A*). The data are plotted for an electrode trajectory that was 50 μm lateral to the cell body, and the penetration moved from dorsal to ventral from the lowest threshold stimulation site (electrode depth = 0 μm) for cathodic stimuli 200 μs in duration. The results show that the model thresholds matched well with the experimental thresholds under conditions that mimicked the experimental setup (Gustafsson and Jankowska 1976) (Fig. 4*A*).

The model neuron innervating the bladder (BLA) in the integrated field-neuron model exhibited changes in threshold relative to electrode position that corresponded with bladder pressures evoked by microstimulation of the S_2 segment (Grill et al. 1999). Both the model and the experiment used charge-balanced, cathodic first, biphasic stimuli 0.1 ms in duration, and the experimental results were obtained with a 100- μA stimulus amplitude (Grill et al. 1999). Pressures evoked in the bladder as a function of electrode depth compared qualitatively with the inverse of the threshold for activation of the BLA model neuron for electrode penetrations along a similar trajectory (Fig. 4*B*). The inverse of the model neuron threshold was used as a proxy for the number of neurons that would be

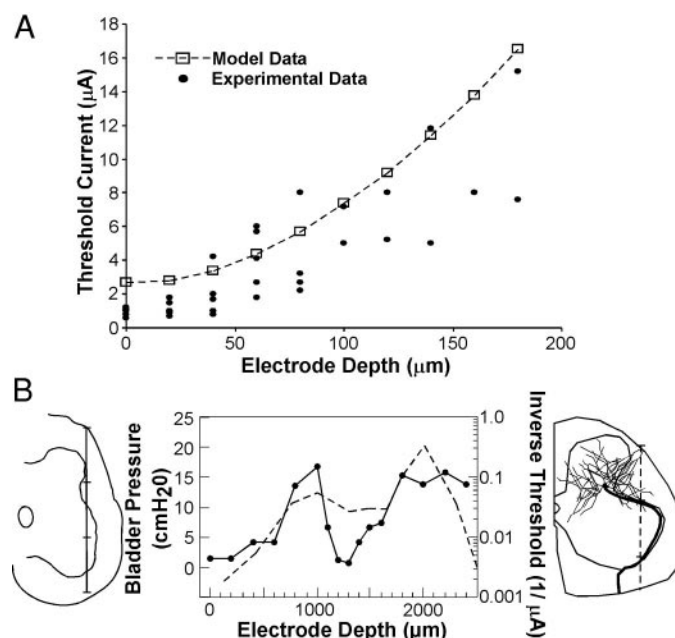


FIG. 4. Comparison of model thresholds for extracellular stimulation to experimental data. *A*: threshold for activation as a function of distance from the external urethral sphincter motoneuron model in a homogenous isotropic medium (tissue conductivity = 0.002 S/cm) compared with experimental data from cat motoneurons (Gustafsson and Jankowska 1976) using monophasic cathodic stimuli 200 μs in duration. *B*: bladder pressures evoked by microstimulation of the S_2 spinal cord as a function of electrode penetration depth (left axes, —) (Grill et al. 1999). Inverse of the threshold (right axes, - - -) as a function of electrode penetration depth for the parasympathetic preganglionic model neuron controlling the bladder with the extracellular electric field calculated by the finite element model of the spinal cord. The electrode paths (1 mm per division) are overlaid on a section of the spinal cord from the experiment (left) and from the model (right). Both the experiment and model used charge-balanced cathode first biphasic stimuli 100 μs in duration.

excited by a particular stimulus amplitude, and it was assumed that the bladder pressure was correlated with the number of activated neurons. This assumption is supported by the experimental results demonstrating the ability to grade bladder pressure, at a particular electrode location, by alterations in the stimulus amplitude (Grill et al. 1999). Points of low threshold in the BLA model near the intermediolateral cell column and near the base of the ventral horn corresponded to regions of high pressures in the experiment (Fig. 4B). Direct quantitative comparisons cannot be made due to geometrical differences in the model and experiment as well as the fact that pressure measurements were the result of activation of many neurons distributed around the electrode. However, the model results do correspond qualitatively with the experimental results, and the stimulus amplitudes necessary for activation of the model neurons correspond with the stimulus amplitude used in the experiment.

Strength-duration relationship of cells and fibers of passage

We examined the effect of changing the stimulus pulse duration on extracellular activation of the EUS, BLA, and FOP neuron models with the standard electrode position in the ventral horn (Fig. 2, D and E). While each neuron had the same threshold for a stimulus pulse duration of 0.1 ms, the FOP had lower thresholds than BLA and EUS for shorter duration pulses and the EUS had the lower thresholds than BLA which had lower thresholds than FOP for longer pulse durations (Fig. 5). In turn, the chronaxie time (τ_{CH}) was different for the different neurons. The local cell (EUS) had the longest τ_{CH} of 408 μ s, the fiber of passage with its cell body near the electrode (BLA) had a τ_{CH} of 222 μ s, and the fiber of passage with its cell body far from the electrode (FOP) had the shortest τ_{CH} of 118 μ s. These values correspond well with previous experimental measurements of extracellular τ_{CH} for local cells (200–700 μ s) and fibers of passage (50–200 μ s) (Nowak and Bullier 1998a; Ranck 1975).

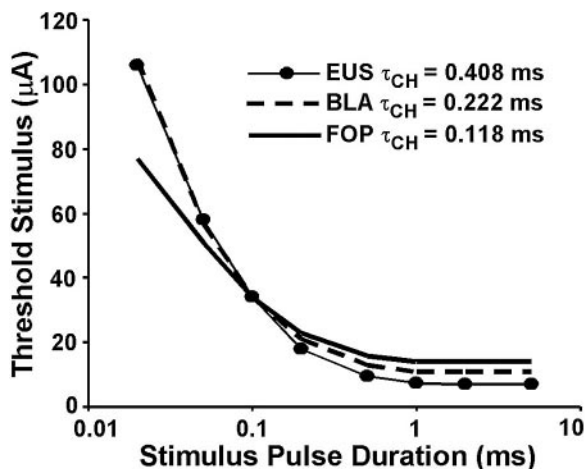


FIG. 5. Strength-duration relationship of local cells and fibers of passage. Threshold for extracellular stimulation of the external urethral sphincter motoneuron (EUS), the neuron innervating the bladder (BLA), and the fiber of passage in the white matter (FOP) in the integrated field-neuron model as a function of stimulus pulse duration of a symmetric charge-balanced biphasic stimulus. The chronaxie time (τ_{CH}) was calculated using a least squares log-log fit to $I_{TH}(PD) = I_{RH} * [1 + (\tau_{CH}/PD)]$, where I_{TH} is the threshold current, I_{RH} is the rheobase current, and PD is the pulse duration (McIntyre and Grill 1998).

Frequency-dependent neuronal output of cells and fibers of passage

Mammalian neurons exhibit both DAPs and AHPs. The time course of these afterpotentials is different in the cell body and axon (Barrett et al. 1980; David et al. 1995; Zengel et al. 1985), and these afterpotentials affect the threshold for generation of subsequent impulses (McIntyre et al. 2002). We hypothesized that differences in the post-action potential excitability of cells and axons could be exploited to enhance selectivity by the appropriate choice of stimulus frequency. Figure 6 shows the response of the EUS neuron (local cell) compared with the response of the FOP to 50- and 125-Hz symmetrical biphasic stimulus trains at 35 μ A. Both the local cell and fiber of passage fired in response to the first stimulus in both trains. Subsequent stimuli in the 50-Hz train fell within the AHP (period of decreased the excitability) of the local cell and fiber of passage. As a result, the neurons were unable to follow the stimuli in at a 1:1 ratio, and the local cell and fiber of passage generated propagating action potentials in response to 33% and 43% of the stimuli, respectively. When the stimulus frequency was increased to 125 Hz once again, both the cell and fiber of passage fired in response to the first stimulus. Subsequent stimuli fell within the DAP (period of increased excitability) of the fiber, and it followed the stimulus frequency at 100%. However, the stimuli fell within a period of decreased excitability of the cell, and it generated action potentials in response to only 14% of the stimuli. These results demonstrate that modulation of the frequency of the stimulus train can enhance selectivity between activation of cells and fibers of passage within the CNS.

Influence of stimulus waveform and frequency on selectivity

Our previous work showed that alterations in the stimulus waveform could enhance selectivity between neuronal populations (McIntyre and Grill 2000). We measured the output of three different neurons in the vicinity of the electrode in response to trains of 25- to 150-Hz stimuli for three different stimulus waveforms (Fig. 7). Maps of the percent of stimuli that generated propagating action potentials during the stimulus train as a function of stimulus amplitude and frequency were generated for the EUS, BLA, and FOP neurons. At high stimulation frequencies, symmetrical charge-balanced biphasic cathodic phase first stimuli generated preferential activation of the FOP compared with the other two neurons (BLA, EUS), while their outputs were similar at low frequencies (Fig. 7A).

Selectivity between the local cell (EUS) and the passing fibers (BLA, FOP) was improved using asymmetrical charge-balanced biphasic stimuli. When an asymmetrical charge-balanced biphasic cathodic phase first stimulus waveform was used, there was a decrease in the threshold for activation of the local cell and an increase in the threshold to activate either passing fiber. For stimulus amplitudes between 35 and 50 μ A, the local cell (EUS) fired at 100%, and there was no activation of either the local (BLA) or passing (FOP) fibers (Fig. 7B). When an asymmetrical charge-balanced biphasic anodic phase first stimulus waveform was used, there was a decrease in the threshold to activate both the local (BLA) and passing (FOP) fibers and an increase in the threshold to activate the local cell (Fig. 6C). For stimulus amplitudes between 38 and 50 μ A,

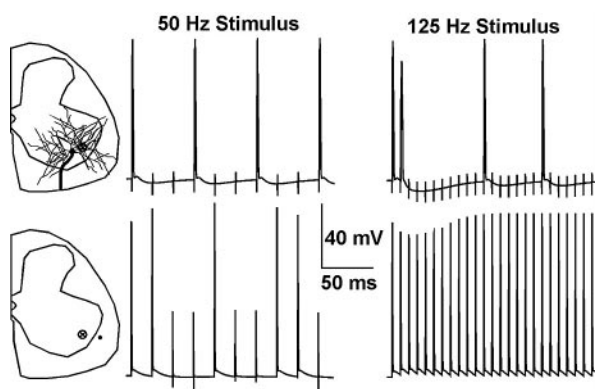


FIG. 6. Stimulus frequency-dependent neural output. Transmembrane potential as a function of time obtained using the integrated field-neuron model. Charge-balanced cathodic phase first symmetrical biphasic 35- μ A stimuli (100- μ s pulse duration for each phase, no interphase delay) were used to activate a neuron with its cell body near the electrode (top) and a fiber of passage (bottom) with stimulus frequencies of 50 Hz (left) and 125 Hz (right). The threshold for activation of each neuron with a single stimulus was 34 μ A.

both the local (BLA) and passing (FOP) axons fired at 100%, and there was no activation of the local cell (EUS). As with conventional biphasic pulses (Figs. 6 and 7A), selectivity between local (BLA) and passing (FOP) fibers could be enhanced using changes in stimulus frequency. At lower frequencies, both BLA and FOP had similar thresholds; however, at frequencies >50 Hz, near-threshold stimulus amplitudes resulted in 100% output from the FOP and $<20\%$ output from the BLA. Instances of selective activation of local fibers (BLA) over both local cells (EUS) and fibers of passage (FOP) were not observed.

Synaptic influence on extracellular activation of local cells

When using extracellular stimulation to activate local cells, it is possible to excite them directly with the stimulus and/or indirectly alter their excitability via excitation (by the stimulus) of synaptic terminals that make connections on the dendritic arbors of the local cells. Previous experimental results have shown that the thresholds for direct or indirect (*trans*-synaptically evoked) action potential generation in local cells are similar with extracellular sources (Baldissera et al. 1972; Gustafsson and Jankowska 1976). To determine the effects of indirect activation of local cells during extracellular stimulus trains, we developed a model of Ia excitatory input to the motoneuron model using detailed morphological data from the literature (Brown and Fyffe 1978; Burke and Glenn 1996) (Fig. 8). The Ia input model consisted of a 6- μ m-diam myelinated fiber running in the medial dorsal column with a 4- μ m-diam collateral projecting into the dorsal gray matter. The collateral branched into two 3- μ m-diam fibers that each branched into two 2.5- μ m-diam fibers, and each of these branched into two 2- μ m-diam fibers that ended with a 1- μ m-diam stem and a 3- μ m-diam bouton that contacted a dendritic branch of the motoneuron. Alpha functions [$I_{\text{syn}} = g_{\text{syn}} * t/\tau * e^{-(t-\tau)/\tau} * (V_m - E_{\text{syn}})$] were used to describe the postsynaptic current at each of the eight contact sites on the dendritic arbor of the EUS motoneuron model. The parameters of the alpha functions were set such that a composite excitatory postsynaptic potential (EPSP) at the soma matched the sub-maximal Ia EPSP measured experimentally ($g_{\text{syn}} = 0.05 \mu\text{S}$; $\tau = 0.5$ ms; $E_{\text{syn}} = 0$ mV) (Burke 1968; Segev et al. 1990) (Fig. 8A).

During extracellular stimulation with the standard ventral horn electrode location (Fig. 2, D and E), action potentials were evoked at all eight boutons of the Ia input for extracellular stimulus amplitudes $>7 \mu\text{A}$ (symmetrical charge-balanced biphasic stimulus), and the presynaptic fibers followed the stimulus frequency 100% for all the stimulus amplitudes examined. After the onset of extracellular stimulus pulse, there was a 1-ms delay before the onset of the postsynaptic current in the motoneuron. The millisecond delay represented activation of the presynaptic fiber, synaptic vesicle activation, transmitter release, diffusion and binding, and postsynaptic channel activation (Baldissera et al. 1972; Gustafsson and Jankowska 1976; Miles and Wong 1984). The output map of the motoneuron near the electrode with the Ia excitatory input (Fig. 8A) was only slightly different from the map without the synaptic input (Fig. 8D). At a stimulus amplitude of 35 μA , excitatory synaptic input resulted in an average increase in neural output of 4% for stimulus frequencies ranging from 75 to 150 Hz. The

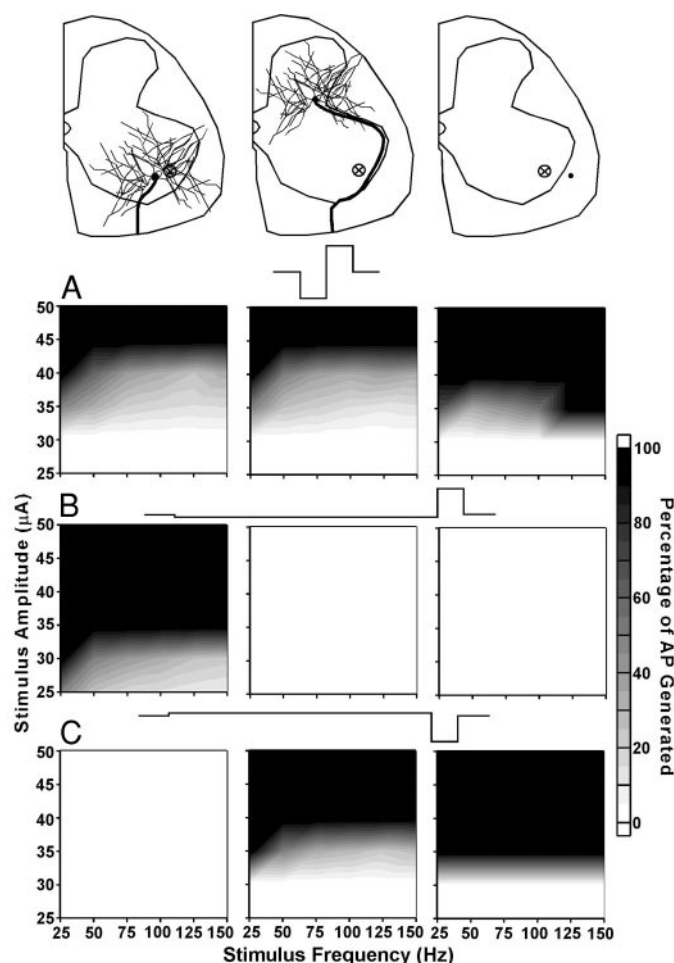


FIG. 7. Neuronal output as a function of stimulus amplitude and frequency. Neuronal output (percentage of stimuli in a 500-ms stimulus train that generated propagating action potentials in the neuron models) was quantified for 3 different neurons using 3 different stimulus waveforms in the field-neuron model. A: neuronal output resulting from a train of charge-balanced cathodic-phase first symmetrical biphasic stimuli (100 μ s per phase). B: neuronal output resulting from a train of charge-balanced asymmetrical biphasic cathodic phase first (1,000- μ s pulse duration), anodic phase second (100- μ s pulse duration) stimuli. C: neuronal output resulting from a train of charge-balanced asymmetrical biphasic anodic phase first (1,000- μ s pulse duration), cathodic phase second (100- μ s pulse duration) stimuli.

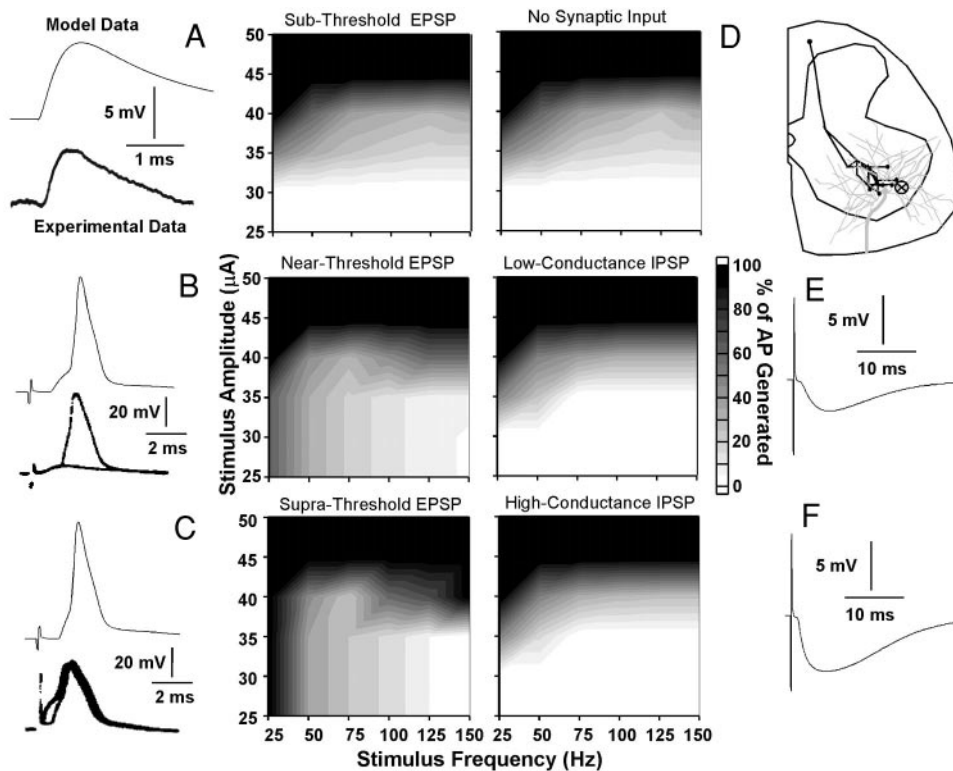


FIG. 8. Influence of synaptic excitation and inhibition on neuronal output. The contour plots show the neuronal output (percentage of stimuli in a 500-ms stimulus train that generated propagating action potentials in the neuron models) generated using charge-balanced cathodic-phase first symmetrical biphasic stimuli (100 μ s per phase) with different types of synaptic inputs. A pictorial representation of the presynaptic axonal arbor terminating on the motoneuron model is shown in the top right corner. **A:** subthreshold indirect activation. Submaximal Ia excitatory input in the model matched well with experimental recording of composite somatic excitatory postsynaptic potentials (EPSPs) (Burke 1968). **B:** near-threshold indirect activation. Model results match the experimental recordings of Gustafsson and Jankowska (1976). **C:** suprathreshold indirect activation. Model results correspond with the experimental recordings of Gustafsson and Jankowska (1976). **E** and **F:** indirect inhibition. Magnitude and time course of the synaptic inhibition induced by the extracellular stimulus as recorded in the soma.

subtle effect of the synaptic inputs on the postsynaptic neuronal output was due to the lack of temporal overlap between the time course of the EPSP and the changes in transmembrane potential generated directly by the stimulus.

The work of Gustafsson and Jankowska (1976) showed that, for dendritic electrode locations, indirect activation of motoneurons could occur at lower stimulus amplitudes than direct activation. Therefore we examined the effect of stimulus frequency on the neuronal output when the *trans*-synaptic influence (EPSP) from the stimulus was near-threshold ($g_{\text{syn}} = 0.2 \mu\text{S}$; Fig. 8B) and suprathreshold ($g_{\text{syn}} = 0.5 \mu\text{S}$) (Fig. 8C) for indirect *trans*-synaptic activation of the motoneuron with single stimuli. With stimulus amplitudes below the threshold for direct excitation (34 μA), the EUS neuron generated action potentials in response to the indirect activation that followed low-frequency stimulus trains in a one-to-one fashion; however, the indirect activation was unable to follow high-frequency stimulation and neuronal output decreased as the stimulus frequency was increased (Fig. 8, B and C). At stimulus amplitudes above the threshold for direct excitation, the EUS neuron with the stimulation induced excitatory synaptic inputs was able to follow higher stimulus frequencies at lower stimulus amplitudes than the EUS neuron without any synaptic input (Fig. 8D).

We also examined the effect of stimulation-induced inhibitory synaptic inputs on the output of the EUS neuron. Inhibitory postsynaptic potentials (IPSPs) traditionally have a longer time course than EPSPs. We implemented IPSPs with alpha functions ($g_{\text{syn}} = 0.2 \mu\text{S}$; $\tau = 3 \text{ ms}$; $E_{\text{syn}} = -80 \text{ mV}$) that produced a peak composite IPSP amplitude of -3 mV in the soma 5 ms after onset and lasted 30 ms (Miles and Wong 1984) (Fig. 8E). The output of the neuron with the stimulation-induced inhibitory synaptic input was reduced in comparison to the output of the neuron without any synaptic input but only

during near threshold stimulation with frequencies $>50 \text{ Hz}$ (Fig. 8, D and E). At a stimulus amplitude of 35 μA , the inhibitory synaptic input resulted in an average decrease in neural output of 16% for stimulus frequencies ranging from 75 to 150 Hz. The minor effect of the inhibitory synaptic input on neuronal output was not dependent on the IPSP synaptic conductance, as a fivefold increase in the conductance ($g_{\text{syn}} = 1.0 \mu\text{S}$) resulted in little change in the neuronal output (Fig. 8F).

DISCUSSION

The objectives of the present study were to develop a quantitative biophysical understanding of the effects of extracellular stimulation within the CNS and to develop and test methods that enabled selective activation of targeted neuronal populations. We used a model of the electric field generated by intraspinal microstimulation coupled to multi-compartment cable models of spinal neurons (field-neuron model) to study activation of CNS neurons with trains of both conventional stimuli and asymmetric stimuli previously developed for selective activation of local cells or fibers of passage (McIntyre and Grill 2000). The results support four main conclusions: asymmetrical stimulus waveform enabled selective activation of either cells near the electrode or fibers of passage, using realistic neuronal orientations and volume conductor fields; the asymmetrical waveforms were at least as effective when used in a stimulus train as they were when delivered as single stimuli; alterations in stimulus frequency altered selectivity because of differences in the afterpotentials and post-action potential excitability between local cells and the fibers of passage; and the threshold for axon terminals in the vicinity of the electrode was lower than the threshold for direct activation of local cells, and thus stimulation induced *trans*-synaptic

inputs influenced the neural response of local cells to extracellular stimuli.

Model limitations

The results obtained with the integrated field-neuron model of intraspinal microstimulation matched well with experimental data but are limited by three general sources. The first set of limitations is related to the neuron models. The models were parameterized based on results from cat lumbar motoneurons as these cells are the most completely characterized cells within the spinal cord. However, the specific properties of the EUS and BLA neurons may not be well represented by lumbar motoneurons. The morphology of EUS motoneurons (Sasaki 1994) is comparable to that of lumbar motoneurons, while preganglionic parasympathetic neurons of the bladder (BLA) have smaller somas (3,009 vs. 4,920 μm^2 for our model) and less extensive dendritic trees (39,138 vs. 269,80 μm^2 for our model) than lumbar motoneurons (Morgan and Ohara 2001). Available electrophysiological data on EUS neurons show they are very similar to the S-type lumbar motoneurons that were used to characterize our models (Hochman et al. 1991; Sasaki 1991). In vivo measurements on cat BLA neurons revealed action potential durations (mean = 5.7 ms) substantially longer than lumbosacral motoneurons, but similar afterhyperpolarization durations (60 ± 12 ms) (de Groat et al. 1982), and neonatal BLA neurons have lower intracellular current thresholds and lower firing rates under tonic depolarization (10–20 imp/s) than lumbar motoneurons (Miura et al. 2000). Thus there are morphological and electrophysiological differences between our model motoneuron and BLA neurons. However, quite different neurons respond very similarly to extracellular stimulation, and changes in excitation patterns with different stimulus parameters were qualitatively similar (Grill and McIntyre 2001; McIntyre and Grill 1999, 2000). Therefore we feel the use of a lumbar motoneuron model was justified as it allowed us to parameterize accurately and test the excitation properties of the model neurons.

While both the motoneuron and myelinated axon models accurately captured the dynamic firing properties recorded experimentally, there are two factors that may limit their ability to reproduce the dynamic firing properties of the neuron at frequencies >100 Hz. The first factor is K^+ accumulation in the periaxonal space of the myelinated axon. During high-frequency activation (300 Hz) of myelinated axons, K^+ concentration in the periaxonal space can increase to the point of reversing the concentration gradient driving internodal K^+ currents. The normally outward fast and slow K^+ currents of the internode reverse to inward currents as a result of changes in the K^+ Nernst potential and generate increased excitability and ectopic discharge (David et al. 1993; Kapoor et al. 1993). This increase in excitability of the myelinated axon during and after very high-frequency stimulation was not included in the present model. However, if included, K^+ accumulation in the periaxonal space would most likely act to enhance the selectivity of fibers of passage over cells seen in Figs. 6 and 7A with high-frequency stimulation.

Another factor that may limit the ability of the model neurons to represent accurately high-frequency dynamic firing is the absence of nonlinear conductances on the modeled dendritic arbor. There are several different types of nonlinear Na^+ ,

K^+ , and Ca^{2+} ion channels on the dendrites of motoneurons (Caldwell et al. 2000; Campbell and Rose 1997; Carlin et al. 2000). The roles of these channels remain unclear, but high-frequency stimulation (200–300 Hz) in combination with serotonin activates a persistent inward current mediated by Ca^{2+} channels on the dendrites that increases the excitability of the motoneuron and in some cases leads to bistability (Hounsgaard and Kiehn 1993; Svirskis et al. 2001). In a previous study, we found that inclusion of nonlinear conductances in the dendrites did not produce substantial differences between the thresholds of cells and fibers of passage for single extracellular stimuli (McIntyre and Grill 2000). However, at higher stimulus frequencies, extracellular stimulation could activate Na^+ and Ca^{2+} conductances on the dendrites acting to enhance the excitability of local cells and altering the selectivity that can be achieved by alterations in the stimulus waveform.

The second set of limitations in this study was related to the calculation of the extracellular electric field produced by the microelectrode. We assumed that the electric field was imposed instantaneously within the medium (i.e., quasi-static conditions) (Plonsey and Heppner 1967), and we used low-frequency values of the conductivity of the tissue medium in the finite-element model. In general, biological conductivities have a small reactive component (Ackman and Seitz 1984; Eisenberg and Mathias 1980). A small increase in conductivity has been observed at higher frequencies (Nicholson 1965; Ranck 1963; Ranck and BeMent 1965); however, >90% of the power in a 100-Hz train of rectangular 100- μs pulses is contained at frequencies <400 Hz. We therefore expect that the assumption of quasi-stationarity was justified.

A second assumption made when calculating the extracellular field was to ignore the impact of the presence of the neuron. If the electrode is in close proximity to the neuron, then the neural structure may distort the electric field within the medium and thus alter the effect of the stimulus on the neuron (Lee and Grill 2001). To account for differences in the extracellular potential across the neuron, the soma was divided into six individual elements rather than treating it as a single lumped element. For the neuron with its cell body close to the electrode (EUS), the difference in the extracellular potential from one side of the soma to the other was 13 mV for a 35- μA stimulus with the standard electrode location used in Figs. 6–8. The use of a multi-compartment soma accounted for the differences in the extracellular potential around the neuron; however, it did not account for the distortion of the extracellular field resulting from the presence of the neuron. We expect this assumption to have introduced only minimal errors in the prediction of excitation for the comparatively large electrode-to-neuron distances considered in this study.

The third set of limitations was related to the representation of the synaptic input on the motoneuron. There exist a total of ~2,500 synaptic contacts on the cell body and dendritic tree of motoneurons (Barnstrom 1993). Our synaptic input model represented only a very small fraction of the total synaptic input to motoneuron (Fig. 7). Consistent with experimental results (Baldissera et al. 1972; Gustafsson and Jankowska 1976), modeled pre-synaptic fibers were excited by stimulus amplitudes below the threshold for direct activation of the local cell. Thus it is likely that a large number of presynaptic fibers will be activated with stimulus amplitudes needed for direct activation, and the effect on the postsynaptic neuron membrane

potential (via postsynaptic potentials) and membrane resistance (via the opening of ion channels) could be substantial. The majority of boutons (~60%) making contact with the cell body and proximal dendrites of the motoneuron are inhibitory, whereas the boutons contacting distal dendrites are split ~50% excitatory, ~50% inhibitory (Barnstrom 1993; Holstege and Calkoen 1990). Therefore during high-frequency extracellular stimulation the overall effect on the cell body may be inhibitory. These effective IPSPs could summate at high frequencies and decrease the excitability of the motoneuron by hyperpolarizing the membrane potential and decreasing the membrane resistance. The effect of this indirect influence of the extracellular stimulus on the postsynaptic neuron could further enhance the selectivity of fibers of passage over cells near the electrode when stimulating at high frequencies but could also limit the ability to activate selectively local cells even with the appropriate stimulus waveform.

However, our results suggest that even large-conductance inhibitory influences on the neuron do not generate substantial changes in the neuronal output (Fig. 8, *E* and *F*). This is because when stimulating local cells with extracellular sources, the site of action potential initiation is in one of the first few nodes of Ranvier (McIntyre and Grill 1999; Nowak and Bullier 1998a,b). As a result, the change in excitability of the cell body and dendrites from the synaptic inhibition is of little importance ~1 mm down the axon. Thus the axonal (and by definition neuronal) output from the stimulus was relatively unaffected by the synaptic inhibition. In addition, during high-frequency stimulation with stimulus amplitudes between 100 and 125% of the threshold for direct activation, and high-conductance synaptic inhibition (Fig. 8*F*), the transmembrane potential recorded at the soma showed little and sometimes no firing while the axon was able to follow the stimulus frequency with much greater efficiency.

Effects of waveform and stimulus frequency on selectivity

Our results indicate that alterations in both the stimulus waveform and stimulus frequency enable selective activation of targeted neuronal populations (Figs. 6 and 7). When high-frequency stimulus trains were used, fibers of passage had greater neuronal output than local cells because of differences in post-action potential excitability. This effect was not seen with the local axon with its cell body relatively close to the electrode (BLA) because the afterpotentials of the cell body were propagated electrotonically to the first few nodes of the myelinated axon. As a result, the afterpotentials of the axon near the cell body were similar to those of the cell body. Therefore our results predict that the increase in selectivity at high frequencies is limited to fibers with their cell bodies far from the electrode (Fig. 7). However, it should be noted that while the selectivity of fibers of passage can be increased with high-frequency stimulation, local cells could still respond to the stimulus, albeit a lower general output (Figs. 6 and 7). The limited output of the local cells from high-frequency stimulation could still be great enough to generate functional activation of their efferent target, and conversely, driving fibers of passage >100 Hz may exceed the physiological limits for those neurons and result in unexpected or unwanted affects. In addition, the firing of the local cell at high stimulus frequencies was not only dependent on its direct excitation characteristics

but also on indirect *trans*-synaptic influences (Fig. 8). In turn, the ability to activate selectively fibers of passage over local cells with high-frequency stimulation is dependent on the net indirect influences on the local cells being inhibitory as predominantly excitatory inputs could enhance activation of the local cells.

Our results demonstrate that a much more robust technique for achieving selective activation of local cells or fibers of passage is alteration of the stimulus waveform. When an asymmetrical charge-balanced biphasic cathodic phase first stimulus waveform designed to activate selectively the cells near the electrode was used (McIntyre and Grill 2000), we saw strong selective activation of the local cell (Fig. 7*B*). Conversely, when an asymmetrical charge-balanced biphasic anodic phase first stimulus waveform designed to activate selectively fibers of passage near the electrode was used (McIntyre and Grill 2000), we saw strong selective activation of fibers of passage (Fig. 7*C*). The long-duration prepulse of these waveforms alters the level of sodium channel inactivation, thereby increasing the excitability in elements hyperpolarized by the prepulse and decreasing the excitability of elements depolarized by the prepulse (Grill and Mortimer 1995; McIntyre and Grill 2000). Antidromic activation of neurons projecting to the region near the electrode (via activation of their axon terminals) also occurred, independent of the stimulus waveform or frequency used, and thus selective activation of either local cells or fibers of passage will be effected by the stimulation induced *trans*-synaptic effects on the local cells (Fig. 8).

Implications for deep brain stimulation

The results of this study, although directed toward intraspinal microstimulation, also provide insight into the effect of stimulus frequency on the arrest of tremor by high-frequency extracellular stimulation of deep brain structures [deep brain stimulation (DBS)]. At higher frequencies (>100 Hz), tremor is suppressed with most patients finding the best results with stimulation frequencies of ~150 Hz (Benabid et al. 1996; Obeso et al. 2001). It has been hypothesized that high-frequency stimulation inhibits tremor by *trans*-synaptic inhibition of local cells via IPSP summation and decreases in the membrane resistance (Benazzouz et al. 1995; Boraud et al. 1996; Dostrovsky et al. 2000). This hypothesis is supported by the fact that GABAergic IPSPs have a time course that matches well with maximal summation occurring at stimulus frequencies where DBS is most effective (Fig. 8, *E* and *F*).

While the mechanisms regulating the therapeutic effects of DBS are not clear, the fact that cathodic stimuli are more effective than anodic stimuli (Benabid et al. 1996), combined with strength-duration results suggest that the targeted neuronal elements are axonal in nature (Ashby et al. 1999; Holsheimer et al. 2000; McIntyre and Grill 2000). The results of this study show that high-frequency stimulation enhances the selective activation of fibers of passage and that axon terminals have lower stimulation thresholds than local cells. However, our results show that the local cell was able to follow high-frequency stimulus trains with 100% output even if the stimulation induced *trans*-synaptic effects were inhibitory (Fig. 8, *E* and *F*). Therefore the results of this study suggest that effects of high-frequency extracellular stimulation within the CNS are activation of fibers of passage, axon terminals, and local cells

near the electrode. If the stimulation-induced *trans*-synaptic effects on the local cells are predominately inhibitory (as is the case in the target nuclei for DBS), then there should be a suppression of underlying activity in the local cells during the inter-stimulus interval as a result of the hyperpolarization of the dendrites and cell body impeding normal synaptic integration. However, the interpretation of suppression of activity during the interstimulus interval to represent block of activity in that nuclei, as seen in experimental recordings (Benazzouz et al. 1995; Boraud et al. 1996; Dostrovsky et al. 2000), does not account for the effects of direct excitation of local cells resulting from the stimulus train.

APPENDIX

The ionic currents of the neural models can be written in the general form of

$$I_{\text{ion}} = g_{\text{ion}}(V_m - E_{\text{ion}})$$

where g_{ion} is the maximum conductance for the individual ion channel (Tables 3 and 4) multiplied by gating variables that range from 0 to 1 (Hodgkin and Huxley 1952). The time and voltage dependence of each gating parameter (ω) is given by

$$\tau_{\omega} = 1/(\alpha_{\omega} + \beta_{\omega})$$

$$d\omega/dt = \alpha_{\omega}(1 - \omega) - \beta_{\omega}\omega = (\omega_{\infty} - \omega)/\tau_{\omega}$$

The time course and magnitude of the activation and inactivation parameters used in the simulations are given in the following text. The membrane dynamics were derived to be representative of neural excitation at 36°C and based on the experimental references given in METHODS and the previous motoneuron modeling work of Booth et al. (1997) and Jones and Bawa (1997). The models were implemented using NEURON v4.3.1 (Hines and Carnevale 1997) and a time step of 0.005 ms. Individuals interested in reproducing the results of this study or using these models in their own work are encouraged to contact us for the appropriate NEURON files and instruction on their use. Times are in milliseconds, voltages are in millivolts, currents are in milliamperes per square centimeter, and concentrations are in millimolar.

Nodal fast sodium current

$$\begin{aligned} I_{\text{Naf}} &= g_{\text{Naf}} * m^3 * h * (V_m - E_{\text{Na}}) \\ \alpha_m &= [6.57 * (V_m + 10.4)] [1 - e^{\{- (V_m + 10.4)/10.3\}}] \\ \beta_m &= [0.304 * (- (V_m + 15.7))] [1 - e^{\{(V_m + 15.7)/9.16\}}] \\ \alpha_h &= [0.34 * (- (V_m + 104))] [1 - e^{\{(V_m + 104)/11\}}] \\ \beta_h &= 12.6 [1 + e^{\{- (V_m + 21.8)/13.4\}}] \end{aligned}$$

Nodal persistent sodium current

$$\begin{aligned} I_{\text{Nap}} &= g_{\text{Nap}} * p^3 * (V_m - E_{\text{Na}}) \\ \alpha_p &= [0.0353 * (V_m + 17)] [1 - e^{\{- (V_m + 17)/10.2\}}] \\ \beta_p &= [0.000883 * (- (V_m + 24))] [1 - e^{\{(V_m + 24)/10\}}] \end{aligned}$$

Nodal slow potassium current

$$\begin{aligned} I_{\text{Ks}} &= g_{\text{Ks}} * s * (V_m - E_{\text{K}}) \\ \alpha_s &= 0.3 [1 + e^{\{(V_m + 43)/-5\}}] \\ \beta_s &= 0.03 [1 + e^{\{(V_m + 80)/-1\}}] \end{aligned}$$

Initial segment fast sodium current

$$\begin{aligned} I_{\text{Naf}} &= g_{\text{Naf}} * m^3 * h * (V_m - E_{\text{Na}}) \\ \alpha_m &= [0.4 * (- (V_m + 60))] [e^{\{- (V_m + 60)/5\}} - 1] \\ \beta_m &= [0.4 * (V_m + 40)] [e^{\{(V_m + 40)/5\}} - 1] \\ \tau_h &= 30 [e^{\{(V_m + 60)/15\}} + e^{\{- (V_m + 60)/16\}}] \\ h_{\infty} &= 1/[1 + e^{\{(V_m + 65)/7\}}] \end{aligned}$$

Initial segment persistent sodium current

$$\begin{aligned} I_{\text{Nap}} &= g_{\text{Nap}} * p^3 * (V_m - E_{\text{Na}}) \\ \alpha_p &= [0.0353 * (V_m + 28.4)] [1 - e^{\{- (V_m + 28.4)/5\}}] \\ \beta_p &= [0.000883 * (- (V_m + 32.7))] [1 - e^{\{(V_m + 32.7)/5\}}] \end{aligned}$$

Initial segment delayed rectifier potassium current

$$\begin{aligned} I_{\text{Kdr}} &= g_{\text{Kdr}} * n^4 * (V_m - E_{\text{K}}) \\ \tau_n &= 5 [e^{\{(V_m + 50)/40\}} + e^{\{- (V_m + 50)/50\}}] \\ n_{\infty} &= 1/[1 + e^{\{(V_m + 38)/-15\}}] \end{aligned}$$

Soma fast sodium current

$$\begin{aligned} I_{\text{Naf}} &= g_{\text{Naf}} * m^3 * h * (V_m - E_{\text{Na}}) \\ \alpha_m &= [0.4 * (- (V_m + 66))] [e^{\{- (V_m + 66)/5\}} - 1] \\ \beta_m &= [0.4 * (V_m + 32)] [e^{\{(V_m + 32)/5\}} - 1] \\ \tau_h &= 30 [e^{\{(V_m + 60)/15\}} + e^{\{- (V_m + 60)/16\}}] \\ h_{\infty} &= 1/[1 + e^{\{(V_m + 65)/7\}}] \end{aligned}$$

Soma delayed rectifier potassium current

$$\begin{aligned} I_{\text{Kdr}} &= g_{\text{Kdr}} * n^4 * (V_m - E_{\text{K}}) \\ \tau_n &= 5 [e^{\{(V_m + 50)/40\}} + e^{\{- (V_m + 50)/50\}}] \\ n_{\infty} &= 1/[1 + e^{\{(V_m + 38)/-15\}}] \end{aligned}$$

Soma calcium dynamics

$$\begin{aligned} [\text{Ca}]_o &= 2 \\ [\text{Ca}]_i(t=0) &= 0.0001 \\ d[\text{Ca}]_i/dt &= 0.01 * (- (I_{\text{CaN}} + I_{\text{CaL}}) - (4 * [\text{Ca}]_i)) \\ E_{\text{Ca}} &= [(1000 * R * 309.15)/(2 * F)] * \ln([\text{Ca}]_o/[\text{Ca}]_i) \end{aligned}$$

Soma N-type calcium current

$$\begin{aligned} I_{\text{CaN}} &= g_{\text{CaN}} * m^2 * h * (V_m - E_{\text{Ca}}) \\ \tau_m &= 15 \\ m_{\infty} &= 1/[1 + e^{\{(V_m + 32)/-5\}}] \\ \tau_h &= 50 \\ h_{\infty} &= 1/[1 + e^{\{(V_m + 50)/5\}}] \end{aligned}$$

Soma L-type calcium current

$$\begin{aligned} I_{\text{CaL}} &= g_{\text{CaL}} * p * (V_m - E_{\text{Ca}}) \\ \tau_p &= 400 \end{aligned}$$

$$p_{\infty} = 1/[1 + e^{(V_m + 55.8)/(-3.7)}]$$

Soma calcium-activated potassium current

$$I_{K(Ca)} = g_{K(Ca)} * ([Ca]_i^2 / ([Ca]_i^2 + 0.014^2)) * (V_m - E_K)$$

This work was supported by a grant from the National Science Foundation (BES-9709488) and Grants NS-40894 and HD-07500 from the National Institutes of Health.

REFERENCES

- ACKMAN JJ AND SEITZ MA. Methods of complex impedance measurement in biologic tissue. *CRC Crit Rev Biomed Eng* 11: 281–311, 1984.
- ASHBY P, KIM YJ, KUMAR R, LANG AE, AND LOZANO AM. Neurophysiological effects of stimulation through electrodes in the human subthalamic nucleus. *Brain* 122: 1919–1931, 1999.
- BALDISSERA F, LUNDBERG A, AND UDO M. Stimulation of pre- and postsynaptic elements in the red nucleus. *Exp Brain Res* 15: 151–167, 1972.
- BARBEAU H, MCCREA DA, O'SONOVAN MJ, ROSSIGNOL S, GRILL WM, AND LEMAY MA. Tapping into spinal circuits to restore motor function. *Brain Res Rev* 30: 27–51, 1999.
- BARNSTROM T. Quantitative synaptology of functionally different types of cat medial gastrocnemius α -motoneurons. *J Comp Neurol* 330: 439–454, 1993.
- BARRETT EF, BARRETT JN, AND CRILL WE. Voltage-sensitive outward currents in cat motoneurons. *J Physiol (Lond)* 304: 251–276, 1980.
- BARRETT JN AND CRILL WE. Voltage clamp of cat motoneuron somata: properties of the fast inward current. *J Physiol (Lond)* 304: 231–249, 1980.
- BASSER PJ AND ROTH BJ. New currents in electrical stimulation of excitable tissues. *Annu Rev Biomed Eng* 2: 377–397, 2000.
- BENABID AL, POLLAK P, GAO D, HOFFMANN D, LIMOUSIN P, GAY E, PAYEN I, AND BENAZZOZOU A. Chronic electrical stimulation of the ventralis intermedius nucleus of the thalamus as a treatment of movement disorders. *J Neurosurg* 84: 203–214, 1996.
- BENAZZOZOU A, PIALLAT B, POLLAK P, AND BENABID AL. Responses of substantia nigra pars reticulata and globus pallidus complex to high-frequency stimulation of the subthalamic nucleus in rats: electrophysiological data. *Neurosci Lett* 189: 77–80, 1995.
- BORAUD T, BEZARD E, BIOULAC B, AND GROSS C. High frequency stimulation of the internal Globus Pallidus (GPi) simultaneously improves parkinsonian symptoms and reduces the firing frequency of GPi neurons in the MPTP-treated monkey. *Neurosci Lett* 215: 17–20, 1996.
- BOOTH V, RINZEL J, AND KIEHN O. Compartmental model of vertebrate motoneurons for Ca^{2+} -dependent spiking and plateau potentials under pharmacological treatment. *J Neurophysiol* 78: 3371–3385, 1997.
- BROWN AG AND FYFFE RE. The morphology of group Ia afferent fibre collaterals in the spinal cord of the cat. *J Physiol (Lond)* 274: 111–127, 1978.
- BURKE RE. Group Ia synaptic input to fast and slow twitch motor units of cat triceps surae. *J Physiol (Lond)* 196: 605–630, 1968.
- BURKE RE AND GLENN LL. Horseradish peroxidase study of the spatial and electrotonic distribution of group Ia synapses on type-identified ankle extensor motoneurons in the cat. *J Comp Neurol* 372: 465–485, 1996.
- CALDWELL JH, SCHALLER KL, LASHER RS, PELES E, AND LEVINSON SR. Sodium channel Na(v)1.6 is localized at nodes of Ranvier, dendrites, and synapses. *Proc Natl Acad Sci USA* 97: 5616–5620, 2000.
- CAMPBELL DM AND ROSE PK. Contribution of voltage-dependent potassium channels to the somatic shunt in neck motoneurons of the cat. *J Neurophysiol* 77: 1470–1486, 1997.
- CARLIN KP, JONES KE, JIANG Z, JORDAN LM, AND BROWNSTONE RM. Dendritic L-type calcium currents in mouse spinal motoneurons: implications for bistability. *Eur J Neurosci* 12: 1635–1646, 2000.
- CATTERALL WA. Localization of sodium channels in cultured neural cells. *J Neurosci* 1: 777–783, 1981.
- CLEMENTS JD AND REDMAN SJ. Cable properties of cat spinal motoneurons measured by combining voltage clamp, current clamp, and intracellular staining. *J Physiol (Lond)* 409: 63–87, 1989.
- CULLHEIM S, FLESHMAN JW, GLENN LL, AND BURKE RE. Membrane area and dendritic structure in type-identified triceps surae alpha motoneurons. *J Comp Neurol* 255: 68–81, 1987.
- CULLHEIM S AND KELLERER JO. A morphological study of the axons and recurrent axon collaterals of cat sciatic alpha-motoneurons after intracellular staining with horseradish peroxidase. *J Comp Neurol* 178: 537–557, 1978.
- DAVID G, BARRETT JN, AND BARRETT EF. Activation of internodal potassium conductance in rat myelinated axons. *J Physiol (Lond)* 472: 177–202, 1993.
- DAVID G, MODNEY B, SCAPPATICCI KA, BARRETT JN, AND BARRETT EF. Electrical and morphological factors influencing the depolarizing afterpotential in rat and lizard myelinated axons. *J Physiol (Lond)* 489: 141–157, 1995.
- DE GROAT WC, BOOTH AM, MILNE RJ, AND ROPPOLO JR. Parasympathetic preganglionic neurons in the sacral spinal cord. *J Auton Nerv Sys* 5: 22–43, 1982.
- DOSTROVSKY JO, LEVY R, WU JP, HUTCHISON WD, TASKER RR, AND LOZANO AM. Microstimulation-induced inhibition of neuronal firing in human globus pallidus. *J Neurophysiol* 84: 570–574, 2000.
- EISENBERG RS AND MATHIAS RT. Structural analysis of electrical properties of cells and tissues. *CRC Crit Rev Bioeng* 4: 203–232, 1980.
- FABRICIUS C, BERTHOLD CH, AND RYDMARK M. Dimensions of individual alpha and gamma motor fibers in the ventral funiculus of the cat spinal cord. *J Anat* 184: 319–333, 1994.
- FLESHMAN JW, SEGEV I, AND BURKE RB. Electrotonic architecture of type-identified alpha-motoneurons in the cat spinal cord. *J Neurophysiol* 60: 60–85, 1988.
- GISZTER SF, MUSSA-IVALDI FA, AND BIZZI E. Convergent force fields organized in the frog's spinal cord. *J Neurosci* 13: 467–491, 1993.
- GRILL WM, BHADRA N, AND WANG B. Bladder and urethral pressures evoked by microstimulation of the sacral spinal cord in cats. *Brain Res* 836: 19–30, 1999.
- GRILL WM AND MCINTYRE CC. Extracellular excitation of central neurons: implications for the mechanisms of deep brain stimulation. *Thal Rel Sys* 1: 269–277, 2001.
- GRILL WM AND MORTIMER JT. Stimulus waveforms for selective neural stimulation. *IEEE Eng Med Biol* 14: 375–385, 1995.
- GUSTAFSSON B AND JANKOWSKA E. Direct and indirect activation of nerve cells by electrical pulses applied extracellularly. *J Physiol (Lond)* 258: 33–61, 1976.
- HINES ML AND CARNEVALE NT. The NEURON simulation environment. *Neural Comput* 9: 1179–1209, 1997.
- HOCHMAN S, FEDIRCHUK B, AND SHEFCHYK SJ. Membrane electrical properties of external urethral and external anal sphincter somatic motoneurons in the decerebrate cat. *Neurosci Lett* 127: 87–90, 1991.
- HOLSHEIMER J, DEMEULEMEESTER H, NUTTIN B, AND DE SUTTER P. Identification of the target neuronal elements in electrical deep brain stimulation. *Eur J Neurosci* 12: 4573–4577, 2000.
- HOLSTEGE JC AND CALKOEN F. The distribution of GABA in lumbar motoneuronal cell groups. A quantitative ultrastructural study in rat. *Brain Res* 530: 130–137, 1990.
- HOUNSGAARD J AND KIEHN O. Calcium spikes and calcium plateaux evoked by differential polarization in dendrites of turtle motoneurons in vitro. *J Physiol (Lond)* 468: 245–259, 1993.
- HOUNSGAARD J AND MINTZ I. Calcium conductance and firing properties of spinal motoneurons in the turtle. *J Physiol (Lond)* 398: 591–603, 1988.
- HULBERT RJ AND TATOR CH. An in vivo technique for 3-dimensional field mapping in the rodent spinal cord. *J Neurosci Methods* 47: 179–189, 1993.
- IRONS BM. A frontal solution program for finite element analysis. *Int J Num Methods Eng* 2: 5–32, 1970.
- JONES KE AND BAWA P. Computer simulation of the responses of human motoneurons to composite IA EPSPs: effect of background firing rates. *J Neurophysiol* 77: 405–420, 1997.
- KAPOOR R, SMITH KJ, FELTS PA, AND DAVIES M. Internodal potassium currents can generate ectopic impulses in mammalian myelinated axons. *Brain Res* 611: 165–169, 1993.
- LEE DC AND GRILL WM. Polarization of spherical cells by non-uniform electric fields: steady-state analysis. *Ann Biomed Eng* 29: S128, 2001.
- LEE RH AND HECKMAN CJ. Essential role of a fast persistent inward current in action potential initiation and control of rhythmic firing. *J Neurophysiol* 85: 472–475, 2001.
- LI CH, BAK AF, AND PARKER LO. Specific resistivity of the cerebral cortex and white matter. *Exp Neurol* 20: 544–557, 1968.
- MCINTYRE CC AND GRILL WM. Sensitivity analysis of a model of mammalian neural membrane. *Biol Cybern* 79: 29–37, 1998.
- MCINTYRE CC AND GRILL WM. Excitation of central nervous system neurons by nonuniform electric fields. *Biophys J* 76: 878–888, 1999.
- MCINTYRE CC AND GRILL WM. Selective microstimulation of central nervous system neurons. *Ann Biomed Eng* 28: 219–233, 2000.

- MCINTYRE CC AND GRILL WM. Finite element analysis of the current-density and electric field generated by metal microelectrodes. *Ann Biomed Eng* 29: 227–235, 2001.
- MCINTYRE CC, RICHARDSON AG, AND GRILL WM. Modeling the excitability of mammalian nerve fibers: influence of afterpotentials on the recovery cycle. *J Neurophysiol* 84: 995–1006, 2002.
- MIURA A, KAWATANI M, ARAKI I, AND DE GROAT WC. Electrophysiological properties of lumbosacral preganglionic neurons in the neonatal rat spinal cord. *Brain Res* 872: 54–63, 2000.
- MORGAN CW AND OHARA PT. Quantitative analysis of the dendrites of sacral preganglionic neurons in the cat. *J Comp Neurol* 437: 56–69, 2001.
- MILES R AND WONG RK. Unitary inhibitory synaptic potentials in the guinea-pig hippocampus in vitro. *J Physiol (Lond)* 356: 97–113, 1984.
- MILLER CE AND HENRIQUEZ CS. Finite element analysis of bioelectric phenomena. *CRC Crit Rev Biomed Eng* 18: 207–233, 1990.
- NADELHAFT I, DE GROAT WC, AND MORGAN C. Location and morphology of parasympathetic preganglionic neurons in the sacral spinal cord of the cat revealed by retrograde axonal transport of horseradish peroxidase. *J Comp Neurol* 193: 265–281, 1980.
- NICHOLSON C AND FREEMAN JA. Theory of current source-density analysis and determination of conductivity tensor for anuran cerebellum. *J Neurophysiol* 38: 356–368, 1975.
- NICHOLSON PW. Specific impedance of cerebral white matter. *Exp Neurol* 13: 386–401, 1965.
- NOWAK LG AND BULLIER J. Axons, but not cell bodies, are activated by electrical stimulation in cortical gray matter. I. Evidence from chronaxie measurements. *Exp Brain Res* 118: 477–488, 1998a.
- NOWAK LG AND BULLIER J. Axons, but not cell bodies, are activated by electrical stimulation in cortical gray matter. II. Evidence from selective inactivation of cell bodies and axon initial segments. *Exp Brain Res* 118: 489–500, 1998b.
- OBESO JA, OLANOW CW, RODRIGUEZ-OROZ MC, KRACK P, KUMAR R, AND LANG AE. Deep-brain stimulation of the subthalamic nucleus or the pars interna of the globus pallidus in Parkinson's disease. *N Engl J Med* 345: 956–963, 2001.
- PLONSEY R AND HEPPNER D. Considerations of quasistationarity in electrophysiological systems. *Bull Math Biophys* 29: 657–664, 1967.
- PROCHAZKA A, MUSHAWAR VK, AND MCCREERY DB. Neural prostheses. *J Physiol (Lond)* 533: 99–109, 2001.
- PUDENZ RH, BULLARA LA, JACQUES S, AND HAMBRECHT FT. Electrical stimulation of the brain. III. The neural damage model. *Surg Neurol* 4: 389–400, 1975.
- RANCK JB. Specific impedance of rabbit cerebral cortex. *Exp Neurol* 7: 144–152, 1963.
- RANCK JB. Which elements are excited in electrical stimulation of mammalian central nervous system: a review. *Brain Res* 98: 417–440, 1975.
- RANCK JB AND BEMENT SL. The specific impedance of the dorsal columns of the cat: an anisotropic medium. *Exp Neurol* 11: 451–463, 1965.
- RICHARDSON AG, MCINTYRE CC, AND GRILL WM. Modelling the effects of electric fields on nerve fibers: influence of the myelin sheath. *Med Biol Eng Comput* 38: 438–446, 2000.
- SASAKI M. Membrane properties of external urethral and external anal sphincter motoneurons in the cat. *J Physiol (Lond)* 440: 345–366, 1991.
- SASAKI M. Morphological analysis of external urethral and external anal sphincter motoneurons of cat. *J Comp Neurol* 349: 269–287, 1994.
- SAWCZUK A, POWERS RK, AND BINDER MD. Spike frequency adaptation studied in hypoglossal motoneurons of the rat. *J Neurophysiol* 73: 1799–1810, 1995.
- SAFRONOV BV, WOLFF M, AND VOGEL W. Functional distribution of three types of Na^+ channel on soma and processes of dorsal horn neurones of rat spinal cord. *J Physiol (Lond)* 503: 371–385, 1997.
- SCHWINDT PC AND CRILL WE. Factors influencing motoneuron rhythmic firing: results from a voltage-clamp study. *J Neurophysiol* 48: 875–890, 1982.
- SEGEV I, FLESHMAN JW, AND BURKE RE. Computer simulation of group Ia EPSPs using morphologically realistic models of cat alpha-motoneurons. *J Neurophysiol* 64: 648–660, 1990.
- SVIRSKIS G, GUTMAN A, AND HOUNSGAARD J. Electrotonic structure of motoneurons in the spinal cord of the turtle: inferences for the mechanisms of bistability. *J Neurophysiol* 85: 391–398, 2001.
- THOR KB, MORGAN C, NADELHAFT I, HOUSTON M, AND DE GROAT WC. Organization of afferent and efferent pathways in the pudendal nerve of the female cat. *J Comp Neurol* 288: 263–279, 1989.
- TRAUB RD AND LLINAS R. The spatial distribution of ionic conductances in normal and axotomized motoneurons. *Neuroscience* 2: 829–849, 1977.
- VANDERHORST VG AND HOLSTEGE G. Organization of lumbosacral motoneuronal cell groups innervating hindlimb, pelvic floor, and axial muscles in the cat. *J Comp Neurol* 382: 46–76, 1997.
- WARMAN EN, GRILL WM, AND DURAND D. Modeling the effects of electric fields on nerve fibers: determination of excitation thresholds. *IEEE Trans Biomed Eng* 39: 1244–1254, 1992.
- WATSON DF. *Contouring: A Guide to the Analysis and Display of Spatial Data*. Oxford, UK: Elsevier Science, 1999.
- ZENGEL JE, REID SA, SYPERT GW, AND MUNSON JB. Membrane electrical properties and prediction of motor-unit type of medial gastrocnemius motoneurons in the cat. *J Neurophysiol* 53: 1323–1344, 1985.